

Pseudorandom phase masks for superresolution imaging from subpixel shifting

Amit Ashok and Mark A. Neifeld

We present a method for overcoming the pixel-limited resolution of digital imagers. Our method combines optical point-spread function engineering with subpixel image shifting. We place an optimized pseudorandom phase mask in the aperture stop of a conventional imager and demonstrate the improved performance that can be achieved by combining multiple subpixel shifted images. Simulation results show that the pseudorandom phase-enhanced lens (PRPEL) imager achieves as much as 50% resolution improvement over a conventional multiframe imager. The PRPEL imager also enhances reconstruction root-mean-squared error by as much as 20%. We present experimental results that validate the predicted PRPEL imager performance. © 2007 Optical Society of America

OCIS codes: 110.0110, 110.4190, 100.6640, 100.3020.

1. Introduction

Semiconductor detector arrays are rapidly replacing film as the recording medium of choice within many modern imagers.¹ This trend has led to a preponderance of digital cameras in nearly all applications ranging from consumer photography to modern biomedical imaging. Digital imager design, therefore, is becoming an increasingly important activity. Within the traditional (i.e., film-based) design paradigm the optical point-spread function (PSF) is typically viewed as the resolution-limiting element and thus optical designers strive for an impulse-like PSF. Digital imagers, however, may employ photodetectors that are large relative to the extent of the PSF and in such cases the resulting pixel blur and/or aliasing can become the dominant distortion limiting overall imager performance. This is illustrated by Fig. 1(a). This figure is a 1D depiction of the image formed by a traditional camera when two point objects are separated by a subpixel distance. We see that the resulting impulse-like PSFs are imaged onto essentially the same pixel leading to spatial ambiguity and hence

a loss of resolution. In such an imager, the resolution is said to be *pixel limited*.²

The effect depicted in Fig. 1(a) may also be understood by noting that the detector array undersamples the image and therefore produces aliasing. The generalized sampling theorem by Papoulis³ provides a mechanism through which this aliasing distortion can be mitigated. The theorem states that a band-limited signal ($-\Omega \leq \omega \leq \Omega$) can be completely and perfectly reconstructed from the sampled outputs of R nonredundant (i.e., diverse) linear channels, each of which employs a sample rate of $2\Omega/R$ (i.e., each of the R signals is undersampled at $1/R$ the Nyquist rate). This theorem suggests that aliasing distortion can be reduced by combining multiple undersampled and low-resolution images to obtain a high-resolution image. A detailed description of this technique can be found in Borman.⁴ This approach has been used by several researchers in the image processing community^{2,5–9} and was recently adopted for use in the thin observing module with bounded optics (TOMBO) imaging architecture.^{10,11} The TOMBO system was designed to simultaneously acquire multiple low-resolution images of an object through multiple lenslets in an integrated aperture. The resulting collection of low-resolution measurements is then processed to yield a high-resolution image. Within the TOMBO system the multiple nonredundant images were obtained via a diverse set of subpixel shifts. The use of other forms of diversity including magnification, rotation, and defocus has also been discussed.¹² It is important to note that these methods of obtaining measurement diversity do not fully exploit the optical degrees of freedom available to

A. Ashok (ashoka@ece.arizona.edu) and M. A. Neifeld (neifeld@ece.arizona.edu) are with the Department of Electrical and Computer Engineering, 1230 East Speedway Boulevard, University of Arizona, Tucson, Arizona 85721, USA. M. A. Neifeld is also with the College of Optical Sciences.

Received 12 September 2006; revised 23 November 2006; accepted 28 November 2006; posted 6 December 2006 (Doc. ID 74909); published 3 April 2007.

0003-6935/07/122256-13\$15.00/0

© 2007 Optical Society of America

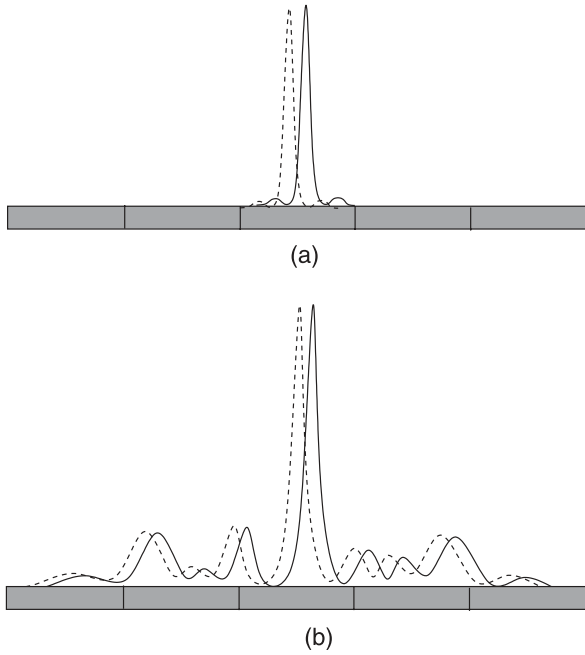


Fig. 1. Schematic depicting the effect of pixel-limited resolution. (a) Optical PSF is impulse-like and (b) engineered optical PSF is extended.

the designer. The approach described herein will utilize PSF engineering to obtain additional diversity from a set of subpixel shifted measurements.

The optical PSF of a digital imager may be viewed as a mechanism for encoding object information so as to better tolerate distortions introduced by the detector array. From this viewpoint an impulse-like optical PSF may be suboptimal.^{13,14} This assertion is made plausible by considering Fig. 1(b), in which we depict an image of two point objects formed using a non-impulse-like PSF. The point objects are spaced as in Fig. 1(a). We see that the use of an extended PSF makes possible the extraction of subpixel position information from the sampled detector outputs. For example, a simple correlation-based processor¹⁵ can yield the PSF centroid–point-source location to subpixel accuracy, given sufficient measurement signal-to-noise ratio (SNR). In this paper, we study the performance of one such extended PSF design obtained by placing a pseudorandom phase mask in the aperture stop of a conventional imager. Our choice of pseudorandom phase mask has been motivated in part by the pseudorandom sequences found in code-division multiple access multiuser communication systems^{16,17} and in part by our previous study,¹⁸ which found pseudorandom phase masks efficient in an information-theoretic sense for imaging sparse volumetric scenes. In the context of multiuser communications, pseudorandom sequences are used to encode the information of each end user. These encoded messages are combined and transmitted over a common channel. The structure of the encoding is then used at the receiver side to extract individual messages from the superposition. In a digital imaging system, the optical PSF serves a similar purpose in

terms of encoding the location of individual resolution elements that comprise the object. The pixels within a semiconductor detector array measure a superposition of response from each resolution element in the object. Further the spatial integration across the finite pixel size of the detector array leads to spatial blurring. These signal transformations imposed by the detector array must be inverted via decoding. In Section 2, we describe the mathematical model of the imaging system and the pseudorandom phase mask used to obtain the extended optical PSF.

2. Imaging Model

Consider a linear model of a digital imaging system. Mathematically, we can represent the system as

$$\mathbf{g} = \mathbf{H}_{cd}f_c + \mathbf{n}, \quad (1)$$

where f_c is the continuous object, \mathbf{g} is the detector-array measurement, \mathbf{H}_{cd} is the continuous-to-discrete imaging operator, and \mathbf{n} is additive measurement noise. For simulation purposes we use a discrete representation \mathbf{f} of the continuous object f_c . This discrete representation \mathbf{f} can be obtained from f_c as follows¹⁹

$$f_i = \int_{S \cap \Phi_i} f_c(\tilde{r}) \phi_i(\tilde{r}) d\tilde{r}^2, \quad (2)$$

where S is the object support, $\{\phi_i\}$ is an analysis basis set, Φ_i is the support of i th basis function ϕ_i and f_i is the i th element of the object vector \mathbf{f} . Note that we obtain an approximation f_a of the original continuous object f_c from its discrete representation \mathbf{f} as follows¹⁹

$$f_a(\tilde{r}) = \sum_{i=1}^N f_i \psi_i(\tilde{r}), \quad (3)$$

where N is the dimension of the discrete object vector and $\{\psi_i\}$ is a synthesis basis set that can be chosen to be the same as the analysis basis set $\{\phi_i\}$. Here we use the *pixel* function to construct our analysis and synthesis basis sets. The pixel function is defined as

$$\phi_i(r) = \frac{1}{\Omega_r} \text{rect}\left(\frac{r - i\Omega_r}{\Omega_r}\right),$$

$$\int_{\Phi_i \cap \Phi_j} \phi_i(r) \phi_j(r) dr^2 = \delta_{ij}, \quad (4)$$

where $2\Omega_r$ is the size of the resolution element in the continuous object that can be accurately represented by this choice of basis set. Note that the pixel functions $\{\phi_i\}$ form an orthonormal basis. We set the object resolution element size equal to the diffraction-limited optical resolution of the imager to ensure that the discrete representation of the object does not incur any loss of spatial resolution. Here we adopt the Rayleigh's criteria²⁰ to define *resolution*. Henceforth, all references to resolution will represent the Rayleigh resolution.

The imaging equation can be modified to include the discrete object representation as follows

$$\mathbf{g} = \mathbf{H}\mathbf{f} + \mathbf{n}, \quad (5)$$

where \mathbf{H} is the equivalent discrete-to-discrete imaging operator: \mathbf{H} is therefore a matrix. The imaging operator \mathbf{H} includes the optical PSF, the detector PSF, and the detector sampling. The vectors \mathbf{f} , \mathbf{g} , and \mathbf{n} are lexicographically arranged one-dimensional representations of the 2D object, image, and noise arrays, respectively.

Consider a diffraction-limited PSF of the form: $h(r) = \text{sinc}^2(r/R)$, with Rayleigh resolution R . The Nyquist sampling theorem requires the detector spacing to be at most $R/2$. When this requirement is met, the imaging operator \mathbf{H} has full rank (condition-number $\rightarrow 1$) allowing a reconstruction of the object up to the optical resolution. However, when the optical PSF has an extent ($2R$) that is smaller than the detector spacing, the image measurement is aliased and the imaging operator \mathbf{H} becomes singular (condition-number $\rightarrow \infty$). Under these conditions the object cannot be reconstructed up to the optical resolution. Also note that due to undersampling, the imaging operator \mathbf{H} is no longer shift invariant but only blockwise shift invariant even if the imaging optics itself is shift invariant.

As mentioned in Section 1, one method to overcome the resolution constraint imposed by the pixel size is to use multiple subpixel shifted image measurements. The subpixel shift δ may be obtained either by a shift in the imager position or through object movement. The i th subpixel shifted image measurement \mathbf{g}_i with shift δ_i can be represented as

$$\mathbf{g}_i = \mathbf{H}_i \mathbf{f} + \mathbf{n}_i, \quad (6)$$

where \mathbf{H}_i represents the imaging operator associated with the subpixel shift δ_i . For a set of K such measurements, we can write the composite image measurement by concatenating the individual vectors as, $\mathbf{g} = \{\mathbf{g}_1 \mathbf{g}_2 \cdots \mathbf{g}_K\}$ and similarly $\mathbf{n} = \{\mathbf{n}_1 \mathbf{n}_2 \cdots \mathbf{n}_K\}$. Now we can express the overall multiframe composite imaging system as

$$\mathbf{g} = \mathbf{H}_c \mathbf{f} + \mathbf{n}, \quad (7)$$

where \mathbf{H}_c is now the composite imaging operator. By combining several subpixel shifted image measurements, the condition number of the composite imaging operator \mathbf{H}_c can be progressively improved and the overall resolution approaches the optical resolution limit. Ideally, the subpixel shifts should be chosen in multiples of D/K so as to minimize the condition number of the forward imaging operator \mathbf{H}_c , where D is the detector spacing.²¹

We are interested in designing an extended optical PSF for use within the subpixel shifting framework. The use of an extended optical PSF can improve the condition number of the imaging operator \mathbf{H}_c . We

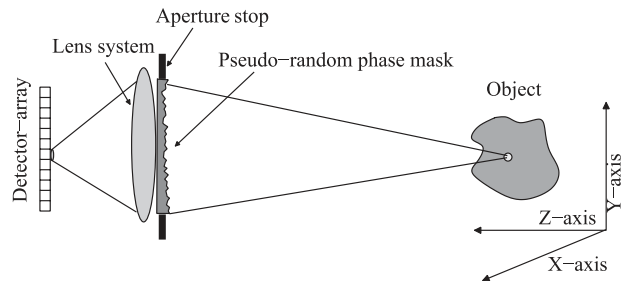


Fig. 2. Imaging system setup used in the simulation study.

consider an extended optical PSF obtained by placing a pseudorandom phase mask in the aperture stop of a conventional imager, as shown in Fig. 2. For simulation purposes, the aperture stop is defined on a discrete spatial grid. Therefore, the pseudorandom phase mask is represented by an array, each element of which corresponds to the phase at given a position on the discrete spatial grid. The pseudorandom phase mask is synthesized in two steps: (1) generate a set of identical independently distributed random numbers distributed uniformly on the interval $[0, \Delta]$ to populate the phase array, and (2) convolve this phase array with a Gaussian filter kernel that is a Gaussian function with standard deviation ρ , sampled on the discrete spatial grid. The resulting set of random numbers define the phase distribution $\Phi(\mathbf{r})$ of the pseudorandom phase mask. The phase mask is thus a realization of a spatial Gaussian random process, which is parameterized by its roughness Δ and correlation length ρ . The autocorrelation function of this phase distribution is given by

$$R_{\Phi\Phi}(r) = \frac{\Delta^2}{12} \exp\left[-\frac{r^2}{4\rho^2}\right]. \quad (8)$$

The resulting incoherent PSF is related to the phase-mask profile $\Phi(\mathbf{r})$ as follows⁹

$$\text{psf}(\mathbf{r}) = \frac{A_c}{(\lambda f)^4} \left| T_{\text{pupil}}\left(-\frac{\mathbf{r}}{\lambda f}\right) \right|^2, \quad (9)$$

$$T_{\text{pupil}}(\boldsymbol{\omega}) = \mathcal{F}\{\exp[j2\pi(n-1)\Phi(\mathbf{r})/\lambda]t_{\text{ap}}(\mathbf{r})\}, \quad (10)$$

where A_c is normalization constant with units of area, n is the refractive index of the lens, f is the back focal length, $t_{\text{ap}}(\mathbf{r})$ is the aperture function, and \mathcal{F} denotes the forward Fourier transform operator.

Figure 3(a) shows a simulated impulse-like PSF and Fig. 3(b) shows an extended PSF resulting from simulating a pseudorandom phase mask with parameters $\Delta = 1.5\lambda_c$ and $\rho = 10\lambda_c$, where λ_c is the operating center wavelength. Here we set $\lambda_c = 550$ nm and the imager $F/\# = 1.8$. Assuming a detector size of $7.5 \mu\text{m}$, the extended PSF spans over roughly six detectors, in contrast with a subpixel extent of $2 \mu\text{m}$ for the impulse-like PSF. The extended PSF will therefore accomplish the desired encoding; however,

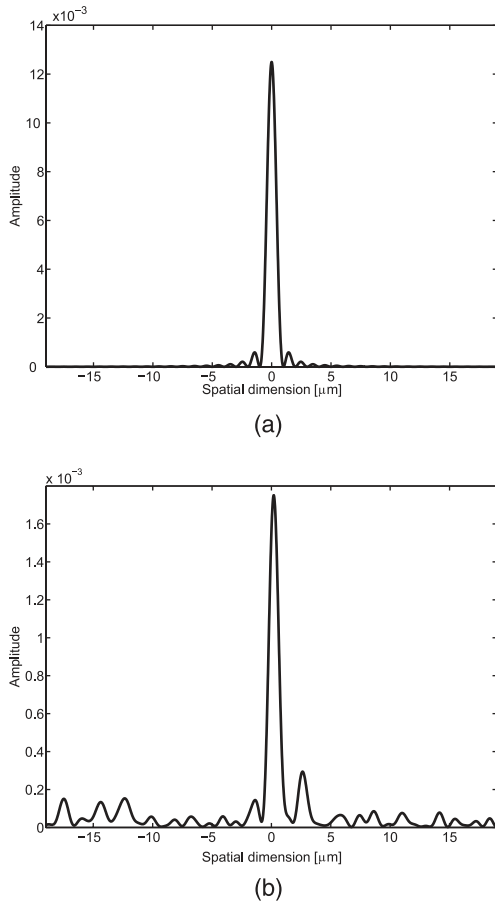


Fig. 3. Example simulated PSFs. (a) Conventional $\text{sinc}^2(\cdot)$ PSF and (b) PSF obtained from PRPEL imager.

it will do so at the cost of measurement SNR. Because the extended PSF is spread over several pixels, its photon count per detector is lower than that for the impulse-like PSF for a pointlike object. Assuming a constant detector noise, the measurement SNR per detector for the extended PSF is thus lower than that of the impulse-like PSF. For more general objects, the extended PSF results in a reduced contrast image with a commensurate SNR reduction, though smaller than for point-like objects. In Section 3, we present a simulation study to quantify the trade-off between the overall imaging resolution and the SNR for two candidate imagers that use multiple subpixel shifted measurements: (a) the conventional imager and (b) the pseudorandom phase-enhanced lens (PRPEL) imager.

3. Simulation Results

For the purposes of the simulation study, we consider only 1D objects and image measurements. The target imaging system has a modest specification with an angular resolution of 0.2 mrad and an angular field of view (FOV) of 0.1 rad. The conventional imager uses a lens of $F/\# = 1.8$ and back focal length 5 mm. We assume that the lens is diffraction limited, and the optical PSF is shift invariant. The detector array in the image plane has a pixel size of $7.5 \mu\text{m}$ with a

full-well capacity (FWC) of 45,000 electrons and a 100% fill factor. We further assume that the imager's spectral bandwidth is limited to 10 nm centered at $\lambda_c = 550 \text{ nm}$. For the PRPEL imager, the only modification is that the lens is followed by a pseudorandom phase mask with parameters Δ and ρ .

We assume a shot-noise limited $\text{SNR} = 23 \text{ dB}$ ($10 \log_{10} \sqrt{\text{FWC}}$) given by the FWC of the detector element. The shot noise is modeled as equivalent additive white Gaussian noise (AWGN) with variance $\sigma^2 = \text{FWC}$. The undersampling factor for this imager is $F = 15$. This implies that for an object vector \mathbf{f} of size $N \times 1$, the resulting image measurement vector \mathbf{g}_i is of size $M \times 1$ where $M = N/F$. For the target imager, these values are $N = 512$ and $M = 34$. Note that the blockwise shift-invariant imaging operator \mathbf{H}_c is of size $KM \times N$.

To improve the overall imager performance, we consider multiple subpixel shifted image measurements or frames. These frames result from moving the imager with respect to the object by a subpixel distance δ_i . Here it is important to constrain the number of photons per frame to ensure a fair comparison among imagers using multiple frames. We have two options: (a) assume that each imager has access to the same finite number of photons and (b) assume that each frame of each imager has access to the same finite number of photons. Option (b) may be physical under certain conditions; however, the results that are obtained will be unable to distinguish between improvements arising from frame diversity versus improvements arising from increased SNR. We therefore utilize option (a) because it is the only option that allows us to study how best to use fixed photon resources. As a result, the photon count for each frame is normalized to F/K in this simulation study.

The inversion of the composite imaging Eq. (7), is based on the optimal linear-minimum mean-squared error (LMMSE) operator \mathbf{W} . The resulting object estimate is given by

$$\hat{\mathbf{f}} = \mathbf{W}\mathbf{g}, \quad (11)$$

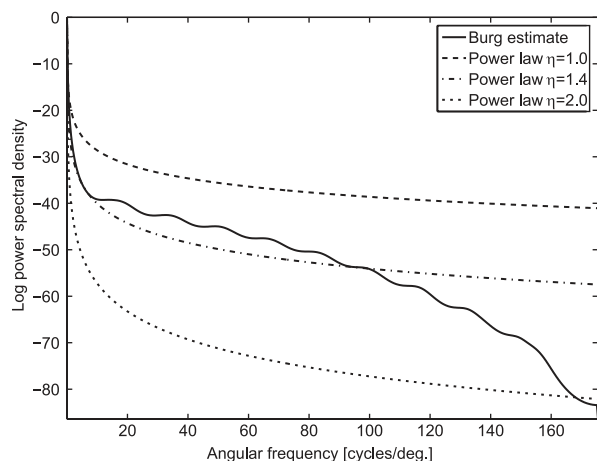
where \mathbf{W} is defined as²²

$$\mathbf{W} = \mathbf{R}_f \mathbf{H}_c^T (\mathbf{H}_c \mathbf{R}_f \mathbf{H}_c^T + \mathbf{R}_n)^{-1}, \quad (12)$$

\mathbf{R}_f is the autocorrelation matrix for the object vector \mathbf{f} and \mathbf{R}_n is the autocorrelation matrix of the noise vector \mathbf{n} . Because the composite imaging operator \mathbf{H}_c is not shift invariant, the LMMSE solution does not reduce to the well known Wiener filter. The noise autocorrelation matrix reduces to a diagonal matrix under the assumption of independent and identically distributed noise and, therefore, can be written as $\mathbf{R}_n = \sigma^2 \mathbf{I}$. The object autocorrelation matrix \mathbf{R}_f incorporates object prior knowledge within the reconstruction process as a regularizing term. Here we obtain the object autocorrelation matrix from a power-law power spectral density (PSD): $1/f^\eta$, that serves as a



(a)



(b)

Fig. 4. Reconstruction incorporates object priors. (a) Object class used for training and (b) PSD obtained from the object class and the best power-law fit used to define the LMMSE operator.

good model for natural images.^{23–25} A power-law PSD was computed to model the class of ten objects shown in Fig. 4(a) chosen to represent a wide variety of scenes (rows and columns of these scenes are used as 1D objects). Figure 4(b) shows several power-law PSDs plotted along with the PSD obtained using Burg's²⁶ method on three objects chosen from the set in Fig. 4(a). The power-law PSD ($\eta = 1.4$) is used to model the PSD of the object class as it is applicable to a wider range of natural images compared with PSD models such as Burg's that are obtained for a specific set of objects. The value of power-law PSD parameter η was obtained by a least-squares fit to Burg's²⁶ PSD estimate.

To quantify the performance of both the PRPEL and the conventional imaging systems, we employ two metrics: (a) Rayleigh resolution and (b) normalized root-mean-square error (RMSE). The Rayleigh resolution of a composite multiframe imager is found by using a point-source object and applying the LMMSE operator to the K image frames. The resulting point-source reconstruction represents the overall PSF of the computational imager and is used to estimate the Rayleigh resolution. A least-squares fit of a diffraction-limited $\text{sinc}^2(\cdot)$ PSF to the overall imager PSF is used to obtain the resolution estimate. Figure 5 illustrates this resolution estimation method with an example of a postprocessed PSF and the associated $\text{sinc}^2(\cdot)$ fit. The second imager performance

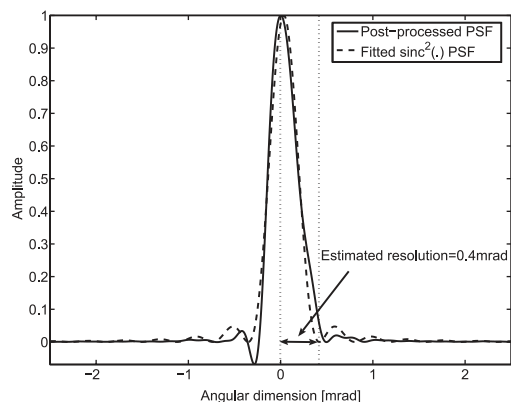


Fig. 5. Rayleigh resolution estimation for multiframe imagers using a $\text{sinc}^2(\cdot)$ fit to the postprocessed PSF.

metric uses RMSE to quantify the quality of a reconstructed object. The RMSE metric is defined as

$$\text{RMSE} = \frac{\sqrt{\langle \|\hat{\mathbf{f}} - \mathbf{f}\|^2 \rangle}}{255} \times 100\%, \quad (13)$$

where 255 is the peak object pixel value. Here, the expectation $\langle \cdot \rangle$ is taken over both the object and the noise ensembles. We have used all columns and rows of the 2D objects shown in Fig. 4(a) to form a set of 1D objects for computing the RMSE metric in the simulation study.

First, we consider the conventional imager. The subpixel shift for each frame is chosen randomly. The performance metrics are computed and averaged over 30 randomly chosen subpixel shift sets for each value of K . Figure 6 shows a plot of the RMSE versus the number of frames K . We see that the RMSE decreases with the number of frames, as expected. This result demonstrates that additional object information is accumulated through the use of diverse (i.e., shifted) channels: as the number of frames increases, the condition number of the composite imaging operator \mathbf{H}_c improves. The reason that the RMSE does not converge to zero for $K = 16$ is because detector noise ultimately limits the minimum reconstruction error.

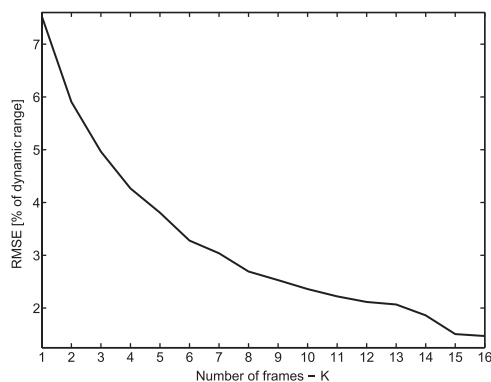


Fig. 6. RMSE versus number of frames for a conventional imager.

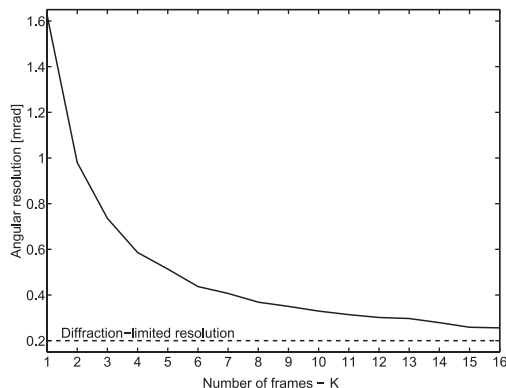


Fig. 7. Rayleigh resolution versus number of frames for a conventional imager.

The resolution of the overall imager is plotted against the number of frames K in Fig. 7. Observe that the resolution improves with increasing K , converging toward the optical resolution limit of 0.2 mrad. Note that the resolution data for $K = 16$ is not equal to the diffraction limit because this data represents an average resolution over a set of random subpixel shift sets. When the subpixel shifts are chosen as multiples of D/F , the resolution achieved for $K = 16$ is indeed equal to the optical resolution limit.

The PRPEL imager employs a pseudorandom phase mask to modify the impulse-like optical PSF. The phase-mask parameters Δ and ρ jointly determine the statistics of the spatial intensity distribution and the extent of the optical PSF. We design an optimal phase mask by setting ρ to a constant ($10\lambda_c$) and finding the value of Δ that maximizes the imager performance for a given K . Figure 8 presents some representative data quantifying imager resolution as a function of Δ with $\rho = 10\lambda_c$ and $K = 3$. This plot shows the fundamental trade-off between the condition number of the imaging operator and the SNR cost. Note that for small values of Δ the PSF is impulse-like. As the value of Δ increases the PSF becomes more diffuse as shown in Fig. 3(b). This results in an improvement in condition number; however, as the PSF becomes more diffuse the photon

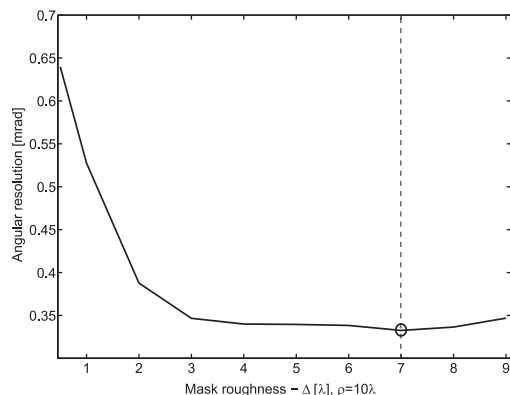


Fig. 8. Example Rayleigh resolution versus mask roughness parameter Δ for $\rho = 10\lambda_c$ and $K = 3$.

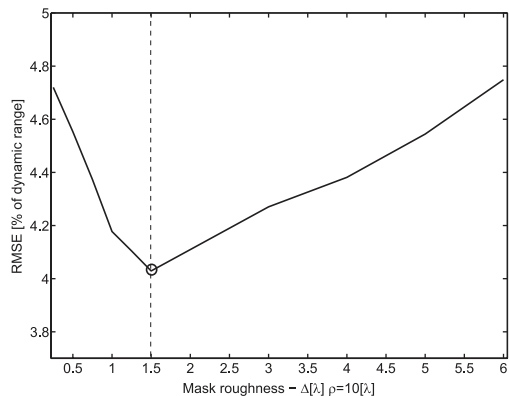


Fig. 9. Example RMSE versus mask roughness parameter Δ for $\rho = 10\lambda_c$ and $K = 3$.

count per detector decreases resulting in an overall decrease in measurement SNR. Figure 8 shows that optimal resolution is achieved for $\Delta = 7\lambda_c$. Figure 9 demonstrates a similar trend in RMSE versus Δ with $\rho = 10\lambda_c$ and $K = 3$. The optimal value of Δ under the RMSE metric is $\Delta = 1.5\lambda_c$. Note that the optimal values of Δ are different for the resolution and RMSE metrics. The resolution of an imager is determined by its spatial-frequency response alone; whereas, the RMSE is dependent on the spatial-frequency response as well as the object statistics. Therefore, the value of Δ that maximizes the resolution metric may result in an imager with a particular spatial-frequency response that may not achieve the minimum RMSE given the object statistics and detector noise. All the subsequent results for the PRPEL imager are obtained for the optimal value of Δ that will therefore be a function of K , σ , and the metric (RMSE or resolution).

Figure 10 presents the resolution performance of both the PRPEL and the conventional imagers as a function of the number of frames K . We note that the PRPEL imager converges faster than the conventional imager. A resolution of 0.3 mrad is achieved with only $K = 4$ by the PRPEL imager in contrast with $K = 12$ for the conventional imager. A plot comparing RMSE performance of the two imagers is

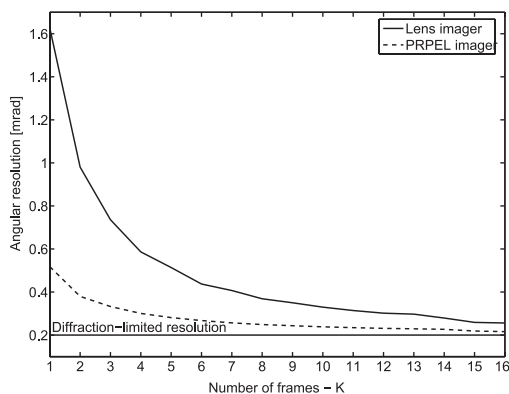


Fig. 10. Rayleigh resolution versus number of frames for both PRPEL and conventional imagers.

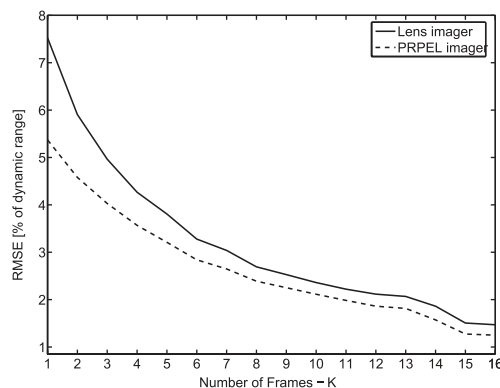


Fig. 11. RMSE versus number of frames for both PRPEL and conventional imagers.

shown in Fig. 11. We note that the PRPEL imager is consistently superior to the conventional imager. For $K = 4$, the PRPEL imager achieves an RMSE of 3.5% as compared with RMSE of 4.3% for the conventional imager.

4. Experimental Results

An experimental demonstration of the PRPEL imager was undertaken in order to validate the performance improvements predicted by simulation. Figure 12 shows the experimental setup along with the relevant physical dimensions. A Santa Barbara Instrument Group (Santa Barbara, Calif., USA) ST2000XM CCD was used as the detector array. The CCD dimensions are 1600×1200 pixels with a detector size of $7.4 \mu\text{m}$ with 100% fill factor and a FWC of 45,000 electrons. The detector output from the CCD is quantized with a 16 bit analog-to-digital convertor yielding a dynamic range of 0–64,000. During the experiment, the CCD is cooled to -10°C , to minimize electronic noise. The experimental imager uses a Fujinon's (Wayne, N.J., USA) CF16HA-1 TV lens operated at $F/\# = 4.0$. A circular holographic diffuser from Physical Optical Corporation (Torrance, Calif., USA) is used as a pseudorandom phase mask. The divergence angle (full width at half-maximum) of the diffuser is 0.1° . A zoom lens with magnification $2.5\times$ is used to decrease the divergence angle of the diffuser. The actual phase statistics of the diffuser are not made available by the manufacturer. Therefore, to relate the physical diffuser to the pseudorandom

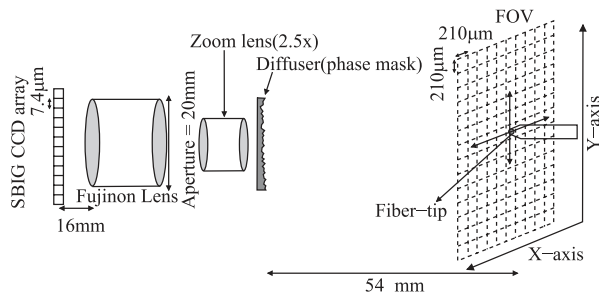


Fig. 12. Schematic of the optical setup used for experimental validation of the PRPEL imager.

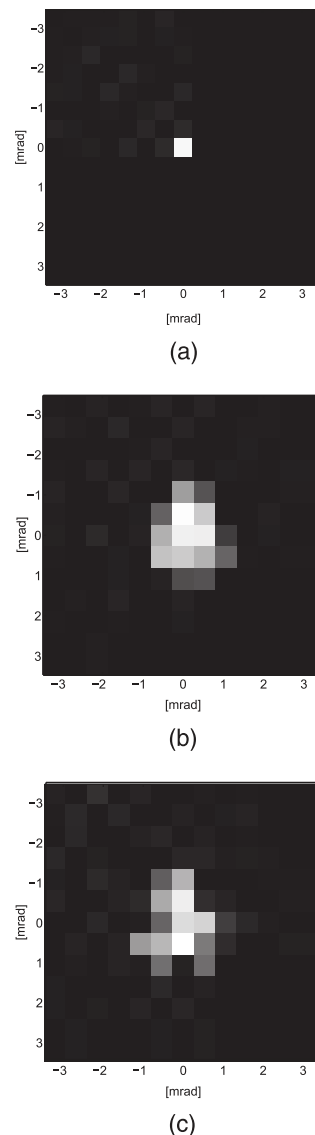


Fig. 13. Experimentally measured PSFs obtained from the (a) conventional imager, (b) PRPEL imager, and (c) simulated PRPEL PSF with phase-mask parameters $\Delta = 2.0\lambda_c$ and $\rho = 175\lambda_c$.

phase-mask model, we compute phase-mask parameters Δ and ρ that yield a PSF similar to the one produced by the physical diffuser. The phase-mask parameters $\Delta = 2.0\lambda_c$ and $\rho = 175\lambda_c$ yield the PSF shown in Fig. 13(c). Comparing this with the PRPEL experimental PSF shown in Fig. 13(b), we note that they are similar in appearance. This comparison although qualitative suggests that the physical diffuser might possess statistics similar to the pseudorandom phase mask model described here.

The Rayleigh resolution of the optical PSF was estimated to be $5 \mu\text{m}$ or 0.31 mrad . This yields an undersampling factor of $F = 3$ along each direction. This implies that a total of $F^2 = 9$ frames are required to achieve the full optical resolution. The FOV for the experiment is $10 \text{ mrad} \times 10 \text{ mrad}$ consisting of 64×64 pixels each of size $0.156 \text{ mrad} \times 0.156 \text{ mrad}$. The highly undersampled nature of the conventional

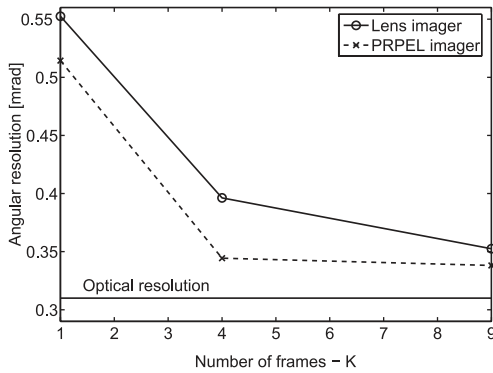


Fig. 14. Experimentally measured Rayleigh resolution versus number of frames for both the PRPEL and conventional imagers.

imager as well as the extended nature of the PRPEL PSF demand careful system calibration. Our calibration apparatus consisted of a fiber-tip point-source mounted on an X-Y translation stage that can be scanned over the object FOV. The 50 μm fiber core diameter in object space yields a 0.6 μm diameter point in image space (system magnification = $\frac{1}{84}\times$), which is much smaller than the detector size of 7.4 μm . Therefore, we can assume that the fiber tip serves as a good point-source approximation for imager calibration purpose. Also note that the exiting radiation from the fiber tip (numerical aperture = 0.22) overfills the entrance aperture of the imager optics by a factor of 12. The motorized translation stage is controlled by a Newport EPS300 (Irvine, Calif., USA) motion controller. The fiber tip is illumi-

nated by a white-light source filtered by a 10 nm bandpass filter centered at $\lambda_c = 535$ nm. The calibration procedure involves scanning the fiber tip over each object pixel position in the FOV and for each such position, recording the discrete PSF at the CCD. We obtain reliable PSF data during calibration by averaging 32 CCD frames to increase the measurement SNR. To obtain PSF data with a particular subpixel shift, the calibration process is repeated after shifting the FOV by that subpixel amount. This calibration data is subsequently used to construct the composite imaging operator \mathbf{H}_c and compute the LMMSE operator \mathbf{W} using Eq. (12). The same calibration procedure is used for both the conventional and the PRPEL imagers.

The experimental PSFs for these two imagers are shown in Fig. 13. The PSF of the conventional imager is seen to be impulse-like; whereas, the PSF of the PRPEL imager has a diffuse or extended shape as expected. The resolution estimation procedure described in Section 3 is employed to estimate the resolution of the two experimental imagers. Figure 14 presents the plot of experimental resolution versus number of frames K . Three data points are obtained from the experiment at $K = 1, 4$, and 9. The subpixel shifts (in micrometers) used for these measurements were: (0, 0) for $K = 1$, (0, 0), (0, 3.7), (3.7, 0), (3.7, 3.7) for $K = 4$, and (0, 0), (0, 2.5), (0, 5), (2.5, 0), (2.5, 2.5), (2.5, 5), (5, 0), (5, 2.5), (5, 5) for $K = 9$. Imager resolution is estimated using test data that are distinct from the calibration data. As predicted in simulation, we see that the PRPEL imager outperforms the con-

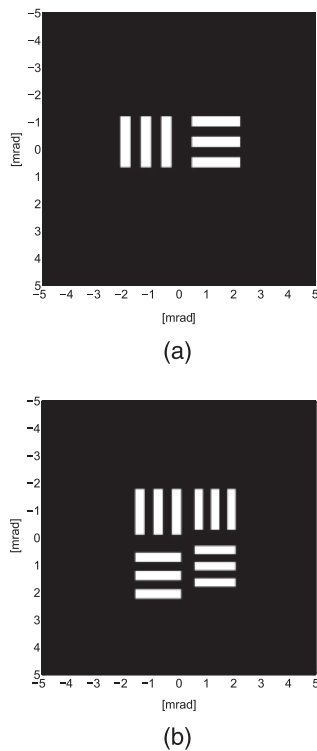


Fig. 15. USAF resolution target (a) group 0 element 1 and (b) group 0 elements 2 and 3.

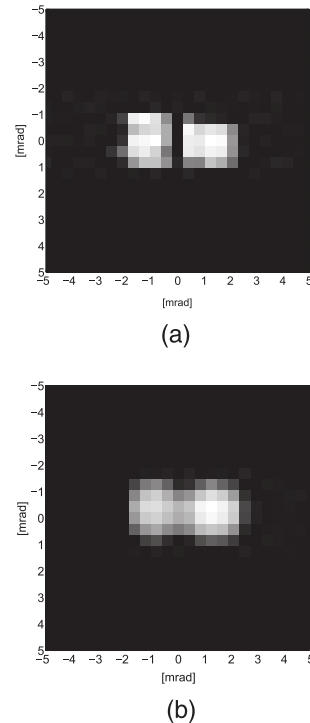


Fig. 16. Raw detector measurements obtained using USAF group 0 element 1 from (a) the conventional imager and (b) the PRPEL imager.

ventional imager at all values of K . We note that the PRPEL resolution nearly saturates by $K = 4$. A maximum resolution gain of 13% is achieved at $K = 4$ by the PRPEL imager relative to the conventional imager. Note that even at $K = 9$, the resolution achieved by both the imagers is slightly poorer than the estimated optical resolution of 0.31 mrad. This can be attributed to errors in the calibration process, which include nonzero noise in the PSF measurements and shift errors due to the finite positioning accuracy of the computer-controlled translation stages.

A U.S. Air Force (USAF) resolution target was used to compare the object reconstruction quality of the two imagers. Because the imager FOV is relatively small ($10 \text{ mrad} \times 10 \text{ mrad}/13.44 \text{ mm} \times 13.44 \text{ mm}$), we used two small areas of the USAF resolution target shown in Figs. 15(a) and 15(b). In Fig. 15(a), the spacing between lines of group 0 element 1 is $500 \mu\text{m}$ in object space or equivalently 0.37 mrad. Similarly in Fig. 15(b), the line spacings for group 0 elements 2 and 3 are 0.33 mrad and 0.30 mrad, respectively. Given the optical resolution of the experimental system, we expect that group 0 element 3 should be

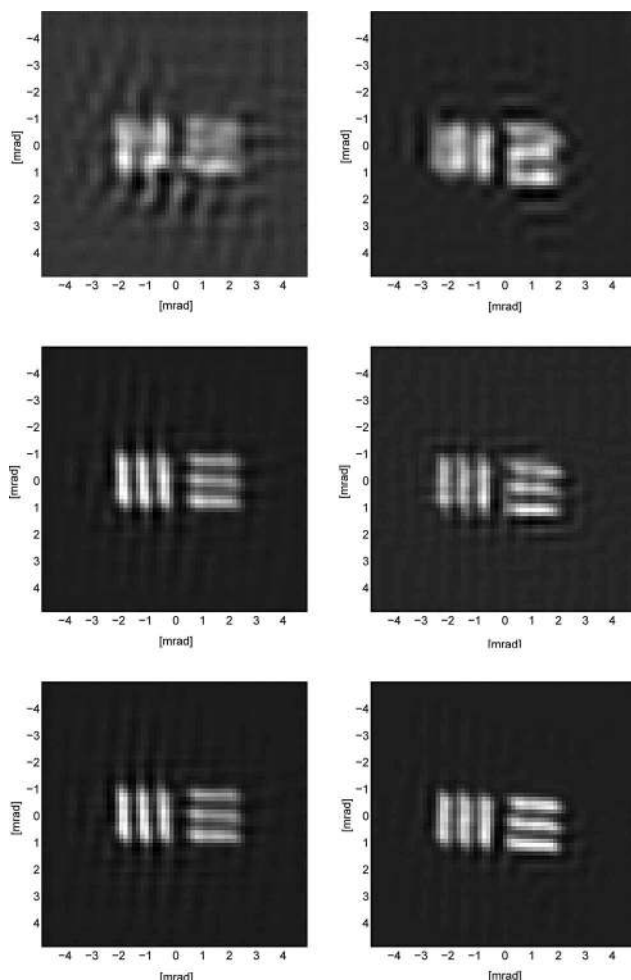


Fig. 17. LMMSE reconstructions of USAF group 0 element 1 with left column for PRPEL imager and right column for conventional imager. Top row, $K = 1$; middle row, $K = 4$; bottom row, $K = 9$.

resolvable by both the conventional and PRPEL imagers.

Figure 16 presents the raw detector measurements of USAF group 0 element 1 from the two imagers. Consistent with the measured degree of undersampling, the imagers are unable to resolve the constituent line elements in the raw data. Figure 17 shows reconstructions from the two multiframe imagers for the same object using $K = 1, 4$, and 9 subpixel shifted frames. We observe that for $K = 1$ neither imager can resolve the object. For $K = 4$, however, the PRPEL imager clearly resolves the lines in the object; whereas, the conventional imager does not resolve them clearly. Figure 18(a) shows a horizontal line scan through the object and LMMSE reconstructions for $K = 4$, affirming our observation that the PRPEL imager achieves superior contrast to that of the conventional imager. For $K = 9$, we note that both imagers resolve the object equally well. Next we consider USAF group 0 elements 2 and 3 object reconstructions that are shown in Fig. 19. As before, for $K = 1$ neither imager can resolve the object. However, for $K = 4$, the PRPEL imager clearly resolves element 2 and barely resolves element 3. In contrast, the conventional imager barely resolves element 2 only. This is also evident in the horizontal line scan of the object and the LMMSE reconstructions shown in Fig. 18(b).

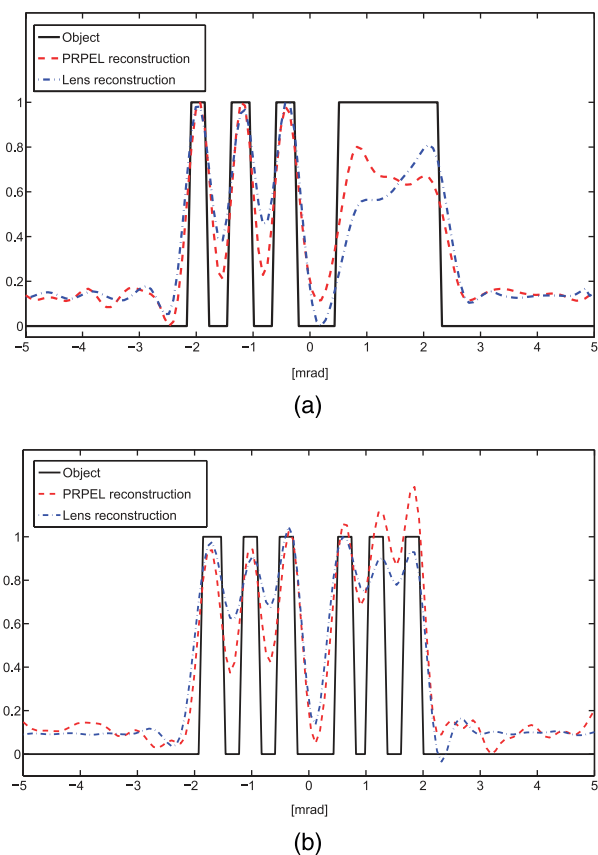


Fig. 18. (Color online) Horizontal line scans through the USAF target and its LMMSE reconstruction for conventional and PRPEL imagers for $K = 4$. (a) Group 0 elements 1 and (b) group 0 elements 2 and 3.

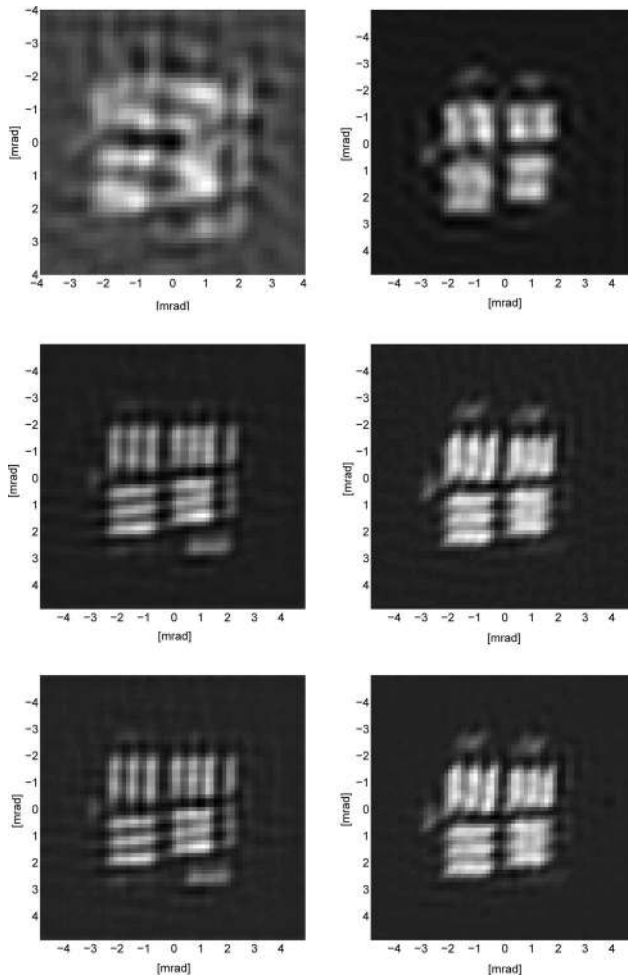


Fig. 19. LMMSE reconstructions of USAF group 0 element 2 and 3 with left column for PRPEL imager and right column for conventional imager. Top row, $K = 1$; middle row, $K = 4$; bottom row, $K = 9$.

Both imagers achieve comparable performance for $K = 9$, completely resolving the object.

We observe that despite having precise channel knowledge, we obtain poor reconstruction results for the case $K = 1$. This points to the limitations of linear reconstruction techniques that cannot include powerful object constraints such as positivity and finite support. However, nonlinear reconstruction techniques such as iterative back projection²⁷ and maximum-likelihood expectation-maximization (MLEM)²⁸ can easily incorporate these constraints. The Richardson–Lucy (RL) algorithm^{29,30} based on the MLEM principle has been shown to be one such effective reconstruction technique. The RL algorithm is a multiplicative iterative scheme where the $k + 1$ th object update denoted by $\hat{\mathbf{f}}^{(k+1)}$ is defined as¹⁹

$$\hat{f}_n^{(k+1)} = \hat{f}_n^{(k)} \frac{1}{s_n} \sum_{m=1}^{KM} \frac{g_m}{(\mathbf{H}_c \hat{\mathbf{f}}^{(k)})_m} (\mathbf{H}_c)_{mn},$$

$$s_n = \sum_{m=1}^{KM} (\mathbf{H}_c)_{mn}, \quad (14)$$

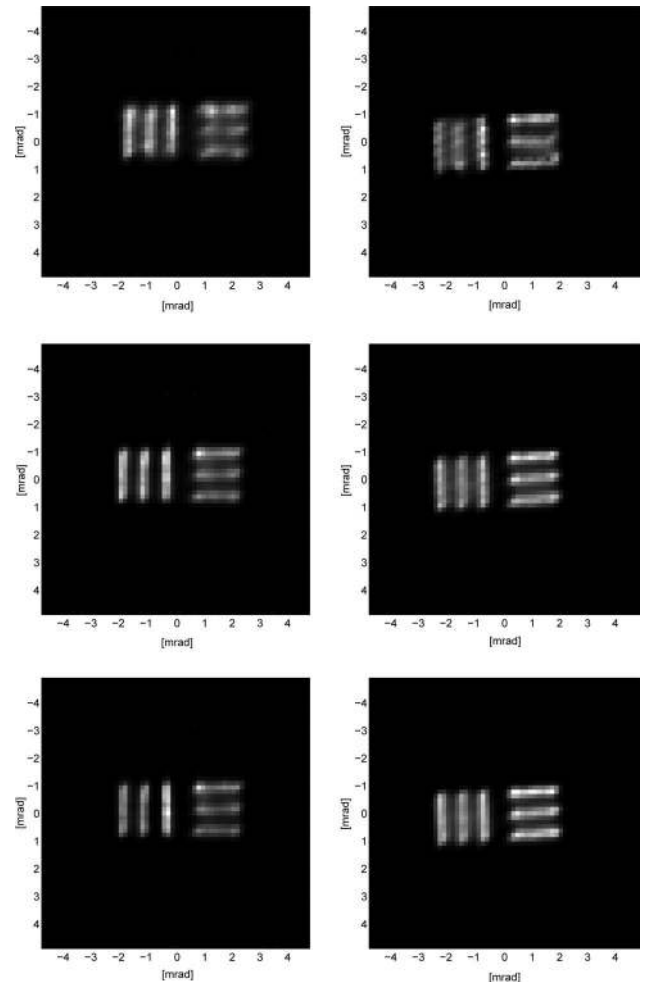


Fig. 20. RL reconstructions of USAF group 0 element 1 with left column for PRPEL imager and right column for conventional imager. Top row, $K = 1$; middle row, $K = 4$; bottom row, $K = 9$.

where the subscript denotes the corresponding element of a vector or a matrix. Note that if all elements of the composite imaging matrix \mathbf{H}_c , the raw image measurement \mathbf{g} , and the initial object estimate $\hat{\mathbf{f}}^{(0)}$ are positive then all subsequent estimates of the object are guaranteed to be positive, thereby achieving the positivity constraint. Further, by setting the appropriate elements of $\hat{\mathbf{f}}^{(0)}$ to 0, we can implement the finite support constraint in the RL algorithm.

We apply the RL algorithm to the experimental data in an effort to improve reconstruction quality, especially for $K = 1$. A constant positive vector is used as an initial object estimate, i.e., $\hat{\mathbf{f}}^{(0)} = \mathbf{c}$ where $c_i = a > 0, \forall i$. Figures 20 and 21 show the RL object reconstructions of the USAF group 0 element 1 and USAF group 0 elements 2 and 3, respectively. As expected, the RL algorithm yields a substantial improvement in reconstruction quality over the LMMSE processor. This improvement is most notable for the $K = 1$ case. In Fig. 20, we observe that the PRPEL imager delivers better results compared with the conventional imager for $K = 1$ and 4. The horizontal line scans in Fig. 22(a) show that the PRPEL imager

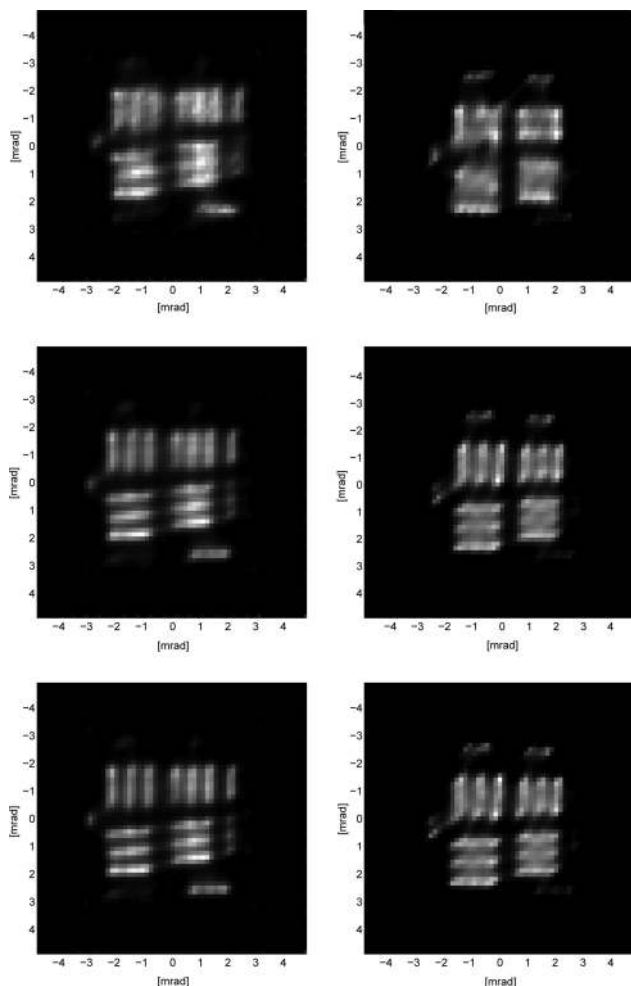


Fig. 21. RL reconstructions of USAF group 0 element 2 and 3 with left column for PRPEL imager and right column for conventional imager. Top row, $K = 1$; middle row, $K = 4$; bottom row, $K = 9$.

maintains a superior contrast compared with the conventional imager for $K = 4$. From Fig. 21, we see that for $K = 1$, the PRPEL imager begins to resolve element 2 whereas the conventional imager still fails to resolve element 2. For $K = 4$, element 2 is clearly resolved and element 3 is just resolved by the PRPEL imager. In comparison, the conventional imager barely resolves element 2. These observations are confirmed by the horizontal line scan plots shown in Fig. 22(b). Overall the experimental reconstruction and resolution results confirm the conclusions drawn from our simulation study; the PRPEL imager offers superior resolution and reconstruction performance compared with the conventional multiframe imager.

5. Imager Parameters

The results reported here have demonstrated the utility of the PRPEL imager. To motivate a more general applicability of the PRPEL approach, there are two important parameters that require further investigation: pixel size and spectral bandwidth. We consider two case studies in which these imaging

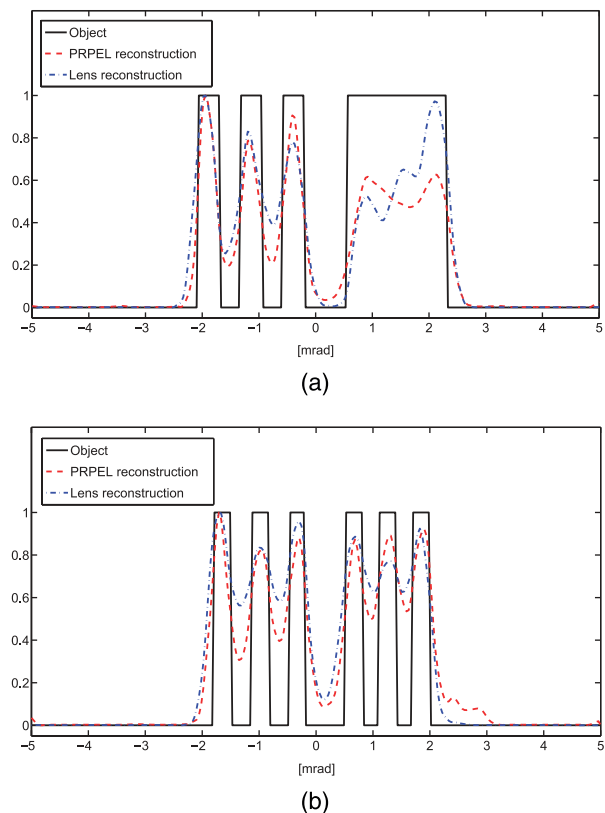


Fig. 22. (Color online) Horizontal line scans through the USAF target and its RL reconstruction for conventional and PRPEL imagers for $K = 4$. (a) Group 0 elements 1 and (b) group 0 elements 2 and 3.

system parameters are modified in order to study their impact on overall imager performance.

A. Pixel Size

Here we consider the effect of smaller pixel size that is typical of complementary metal-oxide semiconductor detectors arrays, now commonly employed in many imagers. Consider a sensor having a pixel size of $3.2 \mu\text{m}$ resulting in a less severe undersampling as compared with the $7.5 \mu\text{m}$ pixel size assumed earlier. This detector has a 100% fill factor and a smaller

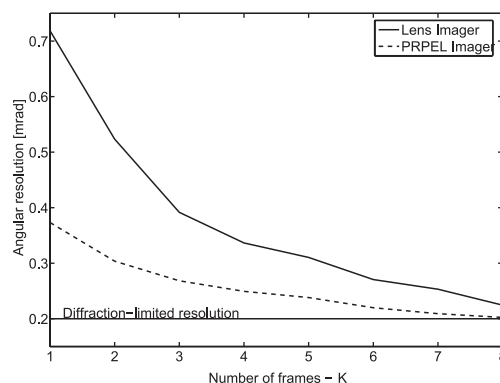


Fig. 23. Rayleigh resolution versus number of frames for multi-frame imagers that employ smaller pixels and lower measurement SNR.

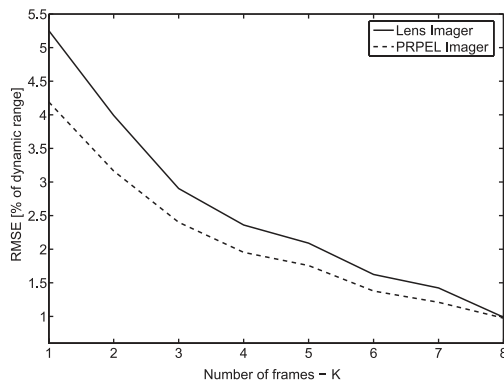


Fig. 24. RMSE versus the number of frames for multiframe imagers that employ smaller pixels and lower measurement SNR.

FWC of 28,000 electrons (lower SNR). All other parameters of the imaging system remain unchanged. The undersampling factor for the new sensor is $F = 7$ and the photon-limited SNR is now 22 dB. We repeat the simulation study of the overall imaging system performance for both the conventional imager and the PRPEL imager. Figure 23 shows a plot of the resolution versus the number of frames for both imaging systems. This plot shows that for $K = 2$, the PRPEL imager achieves a resolution of 0.3 mrad while the conventional imager resolution is only 0.5 mrad. Figure 24 shows the RMSE performance of the two imagers versus number of frames. For $K = 2$, the PRPEL imager achieves a RMSE of 3.2% compared with 4.0% for the conventional imager, an improvement of nearly 20%. From these results we conclude that the PRPEL imager remains a useful option for imagers with CMOS sensors that have smaller pixels and a lower SNR.

B. Broadband Operation

Recall that all our simulation studies have assumed a 10 nm spectral bandwidth so far. In this section, we will relax this constraint and allow the spectral bandwidth to increase to 150 nm, roughly equal to the bandwidth of the green band of the visible spectrum. All other imaging system parameters remain unchanged (using the original $7.5 \mu\text{m}$ sensor). There is

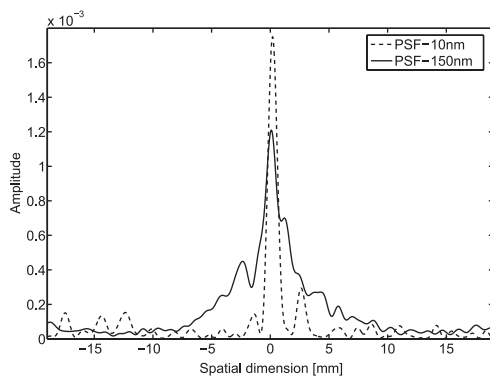


Fig. 25. Optical PSF obtained using PRPEL with both narrow-band (10 nm) and broadband (150 nm) illumination.

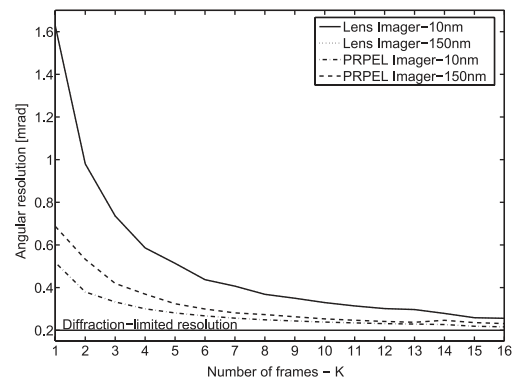


Fig. 26. Rayleigh resolution versus the number of frames for broadband PRPEL and conventional imagers.

a twofold implication of the increased bandwidth. First, because we accept a wider bandwidth, the photon count increases resulting in an improved measurement SNR. Within the PRPEL imager, however, this SNR increase is accompanied by increased chromatic dispersion and a smoothing of the PRPEL PSF. This smoothing results in a worsening of the condition number for the PRPEL imager. To illustrate the dispersion effect, Fig. 25 shows a plot of the extended PRPEL PSF for both the 10 nm and the 150 nm bandwidths. The smoothing of the PSF affects the optical transfer function of the imager by attenuating the higher spatial frequencies. Hence, we can expect a trade-off between the higher SNR and the worsening of the condition number, especially for the PRPEL imaging system. The plot in Fig. 26 shows that the conventional imager resolution is relatively unaffected by broadband operation. The PRPEL imager performance, on the other hand, suffers due to dispersion despite the increase in SNR. Similar trends in RMSE performance can be observed for the two imagers as shown by the plot in Fig. 27. The performance of the broadband PRPEL imager deteriorates relative to narrowband operation for small values of K ; however, note that for medium and large values of K the performance of the PRPEL imager actually improves due to increased SNR.

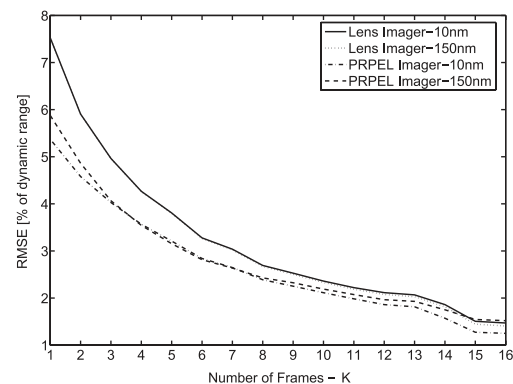


Fig. 27. RMSE versus the number of frames for broadband PRPEL and conventional imagers.

6. Conclusions

We have presented a new approach to overcoming the pixel-limited resolution in digital imagers. We have described a method of engineering the optical PSF in order to better tolerate the undersampling and aliasing that can degrade the performance of digital imagers. Our simulation study of the PRPEL imager predicts substantial performance improvements over a conventional multiframe imager. The PRPEL imager was shown to offer as much as 50% resolution improvement and 20% RMSE improvement as compared to the conventional imager. The experimental results confirmed these predicted performance improvements. We also applied the nonlinear Richardson–Lucy reconstruction technique to the experimental data. The results obtained showed that imager performance is substantially improved with nonlinear techniques. We have also begun to look into alternate parameterizations of phase masks for PSF engineering and initial results suggest that a superposition of sinusoids may provide further improvements in imager performance.³¹

References

1. D. L. Litwiller, "CMOS vs. CCD: maturing technologies, maturing markets," *Photonics Spectra* (August 2005), pp. 54–59.
2. L. Poletto and P. Nicolosi, "Enhancing the spatial resolution of a two-dimensional discrete array detector," *Opt. Eng.* **38**, 1748–1757 (1999).
3. A. Papoulis, "Generalized sampling expansion," *IEEE Trans. Circuits Syst.* **24**, 652–654 (1977).
4. S. Borman, "Topics in multiframe superresolution restoration," Ph.D. dissertation (University of Notre Dame, 2004).
5. S. Farsiu, D. Robinson, M. Elad, and P. Milanfar, "Fast and robust multi-frame super-resolution," *IEEE Trans. Image Process.* **13**, 1327–1344 (2004).
6. N. Galatsanos and R. Chin, "Digital restoration of multichannel images," *IEEE Trans. Acoust., Speech, Signal Process.* **37**, 415–421 (1989).
7. S. P. Kim, N. K. Bose, and H. M. Valenzuela, "Recursive reconstruction of high resolution image from noisy under-sampled multiframes," *IEEE Trans. Acoust., Speech, Signal Process.* **38**, 1013–1027 (1990).
8. H. Ur and D. Gross, "Improved resolution from subpixel shifted pictures," *Comput. Vis. Graph. Image Process.* **54**, 181–186 (1992).
9. M. Elad and A. Feuer, "Restoration of a single superresolution image from several blurred, noisy and undersampled images," *IEEE Trans. Image Process.* **6**, 1646–1658 (1997).
10. J. Tanida, T. Kumagai, K. Yamada, S. Miyatake, K. Ishida, T. Morimoto, N. Kondou, D. Miyazaki, and Y. Ichioka, "Thin observation module by bound optics (TOMBO): concept and experimental verification," *Appl. Opt.* **40**, 1806–1813 (2001).
11. Y. Kitamura, R. Shogenji, K. Yamada, S. Miyatake, M. Miyamoto, T. Morimoto, Y. Masaki, N. Kondou, D. Miyazaki, J. Tanida, and Y. Ichioka, "Reconstruction of a high-resolution image on a compound-eye image-capturing system," *Appl. Opt.* **43**, 1719–1727 (2004).
12. P. M. Shankar, W. C. Hasenplaugh, R. L. Morrison, R. A. Stack, and M. A. Neifeld, "Multiaperture imaging," *Appl. Opt.* **45**, 2871–2883 (2006).
13. M. A. Neifeld and A. Ashok, "Imaging using alternate point spread functions: lenslets with pseudo-random phase diversity," in *Proceedings of the Optical Society of America Topical Meeting: Computational Optical Sensing and Imaging (COSI)* (OSA, 2005), paper CMB1.
14. A. Ashok and M. A. Neifeld, "Engineering the point spread function for superresolution from multiple low-resolution subpixel shifted frames," in *Proceedings of the Optical Society of America Annual Meeting* (OSA, 2005), paper FTHu4.
15. Q. Tian and M. N. Huhns, "Algorithms for subpixel registration," *Comput. Vis. Graph. Image Process.* **35**, 220–233 (1986).
16. S. Verdú, *Multuser Detection* (Cambridge U. Press, 1998), Chap. 2.
17. J. Solmon, Z. Zalevsky, and D. Mendlovic, "Geometric super-resolution by code division multiplexing," *Appl. Opt.* **44**, 32–40 (2005).
18. A. Ashok and M. A. Neifeld, "Information-based analysis of simple incoherent imaging systems," *Opt. Express* **11**, 2153–2162 (2003).
19. H. H. Barrett and K. J. Myers, *Foundations of Image Science* (Wiley-Interscience, 2004), Chaps. 7 and 15.
20. J. W. Goodman, *Introduction to Fourier Optics* (McGraw-Hill, 1996), Chap. 7.
21. E. Y. Lam, "Noise in superresolution reconstruction," *Opt. Lett.* **28**, 2234–2236 (2003).
22. H. C. Andrews and B. R. Hunt, *Digital Image Restoration* (Prentice Hall, 1977).
23. D. J. Tolhurst, Y. Tadmor, and T. Chao, "Amplitude spectra of natural images," *Ophthalmic. Physiol. Opt.* **12**, 229–232 (1992).
24. D. L. Ruderman, "Origins of scaling in natural images," *Vision Res.* **37**, 3385–3398 (1997).
25. D. J. Field and N. Brady, "Visual sensitivity, blur and the sources of variability in the amplitude spectra of natural scenes," *Vision Res.* **37**, 3367–3383 (1997).
26. J. Burg, "Maximum entropy spectral analysis," Ph.D. dissertation (Stanford University, 1975).
27. M. Irani and S. Peleg, "Improving resolution by image registration," *CVGIP: Graph. Models Image Process.* **53**, 231–239 (1991).
28. A. P. Dempster, N. M. Laird, and D. B. Rubin, "Maximum likelihood from incomplete data via the EM algorithm," *J. R. Stat. Soc. Ser. B Methodol.* **39**, 1–38 (1977).
29. L. B. Lucy, "An iterative technique for the rectification of observed distribution," *Astron. J.* **79**, 745–754 (1974).
30. W. H. Richardson, "Bayesian-based iterative method of image restoration," *J. Opt. Soc. Am. A* **56**, 1141–1142 (1972).
31. A. Ashok and M. A. Neifeld, "Recent progress on multidomain optimization for ultrathin cameras," in *Proc. SPIE* **6232**, 62320N (2006).